

# In/Outdoor Organic Solar Cells with Effective Photon-Harvesting by Introducing Light-Amplification Layer with Eco-Friendly QDs

Ji Hyeon Kim, Ye Chan Kim, Ji Youn Kim, Hyoung Seok Lee, Yong Woon Han, Ho Won Lee, and Doo Kyung Moon\*

Quantum dot organic solar cells (QD-OSCs) have received considerable attention because of the luminescent property of QDs and the good miscibility due to the organic ligand in the shell. However, the use of Cd- or Pb-based QDs is limited due to toxicity. Hence, Zn–Cu–In–S/ZnS QDs (ZQs) as nontoxic QDs are used in this study for the light-amplification layer (LAL), consisting of sub-donor (sub-D, D18-Cl) and QDs. The LAL applied between the hole transfer layer (HTL) and bulk heterojunction (BHJ, PM6:BTP-eC9), ensures effective photon amplification and high morphological stability. In particular, the ligands of ZQs constituting LAL interact with D18-Cl and PM6:BTP-eC9 to align molecular orientation and improve interface contact. The sub-D/BHJ structure in which sub-D and BHJ are introduced by layer-by-layer (LBL) coating method solves problems such as morphology degradation and stability degradation due to the complexity of existing ternary system. The sub-D/BHJ, an effective ternary structure, shows a higher performance (17.06%) than the BHJ system (16.66%). Meanwhile, the LAL/BHJ shows not only the highest performance of 17.6% but also outstanding stability (93.6% after 1000 h). This study demonstrates effective energy harvesting through QDs and introduces an optimal QD-OSCs structure strategy for high-efficiency, high-stability OSCs.

## 1. Introduction

The advancement of Internet of Things (IoT) technology and low-carbon green growth policies have accelerated the increase in demand for organic solar cells (OSCs). OSCs are renewable and sustainable energy systems that convert the light energy from solar radiation into electrical energy, consisting of top and bottom electrodes, buffer layers, and active layers. The flexibility, thinness, and good solution process of OSCs based on the physical properties of the organic materials make them applicable in other fields as well. Organic semiconductors have been applied for various purposes, such as indoor power generation and transparent display, as bandgap control is possible according to molecular structural changes.<sup>[1–3]</sup>

Recently, the application technology of building-integrated photovoltaics (BIPVs), vehicle-integrated PVs (VIPVs), indoor PVs (IPVs), and wearable PVs that combine OSCs with IoTs technology has been actively investigated.<sup>[4–6]</sup> To ensure the efficient use of such renewable energy power, not only technological advancements concerning transparency and flexibility but also a high-efficiency and high-stability strategy involving a device structure change are essential.

### 1.1. Device Strategy of Organic Solar Cells


The currently reported high-performance strategy based on device structure changes is as follows: First, multiple layers are joined in a tandem structure to control the energy barrier and broaden the absorption spectrum. Li et al. connected the PM6:AITC and PM6:AITC:BTP-eC9 active systems in a tandem structure and reported 19.4% efficiency.<sup>[7]</sup> In contrast, Hou et al. combined two bulk heterojunctions (BHJs), PBDB-TF:BTP-eC9 and PBDB-TF:GS-ISO, and achieved 20.2% efficiency.<sup>[8]</sup> These two teams produced high-performance devices using tandem structures to improve exciton extraction and extend the absorption range.

Moreover, hybrid structures incorporating various compounds have also been proposed. The most frequently introduced

J. H. Kim, Y. C. Kim, J. Y. Kim, H. S. Lee, Y. W. Han  
Nano and Information Materials Laboratory (NIMs Laboratory)  
Department of Chemical Engineering  
Konkuk University  
120 Neungdong-ro, Gwangjin-gu, Seoul 05029, Republic of Korea

H. W. Lee  
Department of Chemical and Biological Engineering  
Jeju National University  
102 Jejudaehak-ro, Jeju-si, Jeju-do 63243, Republic of Korea

D. K. Moon  
Department of Chemical Engineering  
Konkuk University  
1 Hwayang-dong, Gwangjin-gu, Seoul 143-701, Republic of Korea  
E-mail: dkmoon@konkuk.ac.kr

 The ORCID identification number(s) for the author(s) of this article can be found under <https://doi.org/10.1002/sstr.202300057>.

© 2023 The Authors. Small Structures published by Wiley-VCH GmbH. This is an open access article under the terms of the Creative Commons Attribution License, which permits use, distribution and reproduction in any medium, provided the original work is properly cited.

DOI: 10.1002/sstr.202300057

compounds are inorganic materials, quantum dots (QDs), metal nanowires (NWs), and nanoparticles (NPs). Depending on the introduced compound, various effects can be targeted, such as optical property control, interface control, and electrical property improvement.<sup>[9–12]</sup> Li et al. applied modified ZnO-NPs to the electron transfer layer (ETL) to achieve 18.14% efficiency as the electrical and electron properties were improved via an organic–inorganic heterointerface.<sup>[13]</sup> Meanwhile, Wang et al. proposed QD organic solar cells (QD-OSCs) with the application of CsPbBr<sub>3</sub> or CsPbI<sub>3</sub> perovskite QDs (PQDs) to PM6:Y6-BO-based OSCs, and it reinforced the light absorption properties through PQD scattering, achieving an improved efficiency of 17.1%.<sup>[14]</sup>

In addition, the QD-OSCs strategy through various QDs can improve the efficiency through surface control based on a shell + ligand structure and provide optical advantages based on the emission properties of the core constituting the QDs.<sup>[15–17]</sup> Other available methods include controlling  $E_{\text{gap}}$  and improving stability through active structure change strategies<sup>[18,19]</sup> and concentrating photon energy through light-emitting solar concentrators (LSC).<sup>[20–23]</sup>

Sunlight exhibits a wide range of wavelengths, from ultraviolet (UV) to infrared (IR). Notably, for OSC applications, the key is to determine the performance of conversion from solar energy into electrical energy in various environments and spaces in which the device is placed. The OSC application technology is not installed at the optimal light incident angle like existing solar cells because it is loaded in various spaces such as buildings, vehicles, or low-light environments.<sup>[24–27]</sup> Thus, to harness the maximum energy from the introduced space, a means of effectively using the surplus photon should be developed.<sup>[28]</sup> As a potential solution, this report suggests using QDs consisting of an inorganic compound and an organic ligand.

## 1.2. Properties of ZCIS/ZnS QDs

The QDs generally have a single core, core/shell, or core/shell/ligand configuration. In particular, the core/shell structure is a method of increasing the stability and quantum efficiency of QDs, and the mobility of electron/hole carriers can be controlled depending on how the band gap levels of the core and shell are matched. Research on QDs with an emission effect has accelerated since the 1990s, following a report by Bawendi et al. on a Cd-based QD synthesis method with high quantum efficiency. However, Cd-based QD, which shows excellent emission properties from the beginning to the present, causes environmental problems due to its toxicity. Therefore, the demand for eco-friendly QDs free from heavy toxicity is expanding, and various types of QDs, such as II–VI, II–V, IV–VI, I–III–VI type QDs, carbon QDs, graphene QDs, and PQDs, are being investigated.<sup>[29,30]</sup>

In this study, we focus on the Zn–Cu–In–S/ZnS QDs (ZQs), which take a form in which the ZnS shell with organic ligand surrounds the core consisting of the Zn–Cu–In–S quaternary element. As the ZQs are derived from type I–III–VI Cu–In–S<sub>2</sub> QDs, they are nontoxic while also exhibiting a high absorption coefficient. The ZQs are also easy to fabricate via aqueous phase synthesis, and thus have the advantages of convenient production and ligand control.<sup>[31–33]</sup> The ZQs have a luminescent mechanism due to the energy level produced by Cu defects between the

conduction band (CB) and valence band, in contrast to Cd- or Pb-based QDs emitted from band edge recombination. The principle behind light emission is the generation of an electron from Cu that absorbs photon energy, followed by elimination through nonradioactive or radioactive recombination.<sup>[32,34,35]</sup> Due to the optical advantages, processability, and nontoxic property of ZQs, they are still used in various fields such as white LEDs, biosensing, and solar cell concentrators.<sup>[36–38]</sup> Notably, as the ZQs exhibit a wide emission spectrum through the full width at half-maximum and a high emission intensity in addition to nontoxicity, they are anticipated to be effectively applied to photoelectric devices.

## 1.3. Potential of Quantum Dot Organic Solar Cells

The emitting effect of the core of QDs can lead to additional photons being generated based on the optical properties of QDs, as previously described. As such, QDs can enhance the device performance through surface control of the active system using an organic ligand while simultaneously amplifying the effective light that can be used by the active system based on the light conversion property of the QDs.<sup>[39–41]</sup> Thus, the conditions required to apply QDs to an organic system should ensure a high quantum yield, optical matching with active materials, compatibility, and stability. Notably, to enable ready access by humans, the use of nontoxic QDs is essential, which is one reason that eco-friendly QDs without heavy or toxic elements such as Cd or Pd have been in high demand.

The objectives of this study are to develop a method of effectively applying nontoxic QDs to OSCs and introduce the high-efficiency and high-stability strategy for QD-OSCs according to the interaction between the QDs and organic materials. As introduced, the QDs-hybrid system can be doped in various places, such as the buffer layer or an active layer of OSCs, and it is important to select a location where light energy transfer can occur efficiently. To effectively introduce it into OSCs, it should be fixed in a suitable position according to the particle size or lattice characteristics of QDs and ideally placed in front of an optical path that can take advantage of the optical characteristics of QDs.

## 2. Results and Discussion

### 2.1. Quantum Dots and Device Structure

Figure 1a depicts the prepared ZQ-OSCs concerning the structures of active materials and conventional devices (ITO/PEDOT:PSS(HTL)/light-amplification layer (LAL)/BHJ/PDINN(ETL)/Ag). A LAL consists of sub-donor (sub-D) and light-emitting particles. In the ZQ-OSCs manufactured in this experiment, the LAL consisting of D18-Cl and ZQs is located between the HTL and BHJ. Since ZQs exist on the LAL surface, they are in contact with BHJ, a mixed thin film of PM6:BTP-eC9. The LAL is positioned on the anterior side of light incident path. Therefore, when UV lights are incident on the device, electrons in ZQs are excited. Then the effective photon energy of active materials is amplified, inducing a more effective process of exciton generation and charge transfer at the D/A interface.<sup>[42,43]</sup>

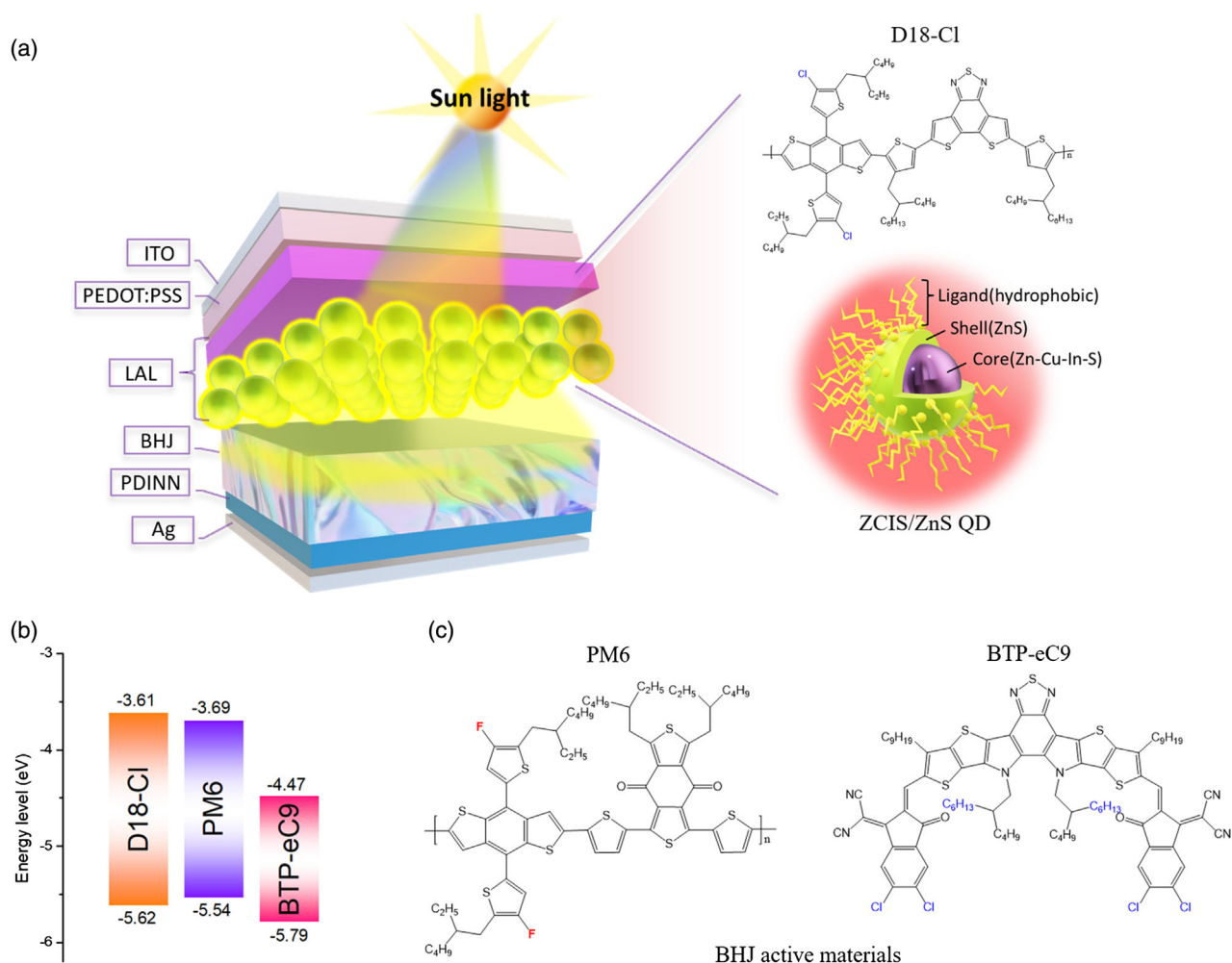


**Figure 1.** a) ZQ-OSCs device structure & light-amplification layer (LAL) materials, b) energy level diagram, and c) bulk heterojunction (BHJ) active materials.

The primary reason for applying ZQs to the sub-D layer rather than BHJ is to prevent morphological reduction of the active layer due to the large particle size of QDs. Another reason is to achieve energy conversion through effective fluorescence resonance energy transfer (FRET) action by positioning ZQs on the anterior side of the light incident path rather than BHJ. The LAL consisting of sub-D and ZQs then forms an effective device structure with an optimal ternary active system, LAL/BHJ, through layer-by-layer (LBL) coating method.<sup>[44,45]</sup> Figure 1b and Table 1 presents the electrical properties of the three active materials. As D18-Cl ( $E_g = 2.01$  eV) is a donor with a wider band gap and deeper HOMO levels than PM6 ( $E_g = 1.85$  eV).<sup>[46]</sup> Hence, a

**Table 1.** Energy levels & optical energy bandgap of active materials.

Formed films	$E_{\text{HOMO}}$ [eV]	$E_{\text{LUMO}}$ [eV]	$E_{g,\text{opt}}$ [eV]
D18-Cl	-5.62	-3.61	2.01
PM6	-5.54	-3.69	1.85
BTP-eC9	-5.79	-4.47	1.32

high concentration of D18-Cl as the sub-D for LAL forms inefficient energy barriers. To resolve this issue, a thin film ( $\approx 10$  nm) with a low concentration of D18-Cl was applied in this study.

In this study, HR-TEM was analyzed for two ZQs with different sizes (Figure 2). The ZQ1 is a smaller one, and the ZQ2 is a larger one grown from the ZQ1. In the measurement of lattice spacing of the two ZQs, similar lattices were shown because they were grown in the same Zn-Cu-In-S core combination. However, in the selected area diffraction (SAD) pattern survey, ZQ1 showed a smaller d-spacing due to differences in growth size. In Figure S1 and Table S1, Supporting Information, when compared through high-resolution transmission electron microscopy (HR-TEM), ZQ1 had a uniform and small particle size, unlike ZQ2, which had a wide histogram distribution.<sup>[47,48]</sup> In addition, the optical properties of two ZQs are analyzed in Figure S2, Supporting Information. Both ZQ1 and ZQ2 were excited in the UV region ( $< 300$  nm) and emitted at 500 nm with 78.25% quantum yield (QY) and 700 nm with 28.21% QY, respectively. Based on this analysis, a uniform and high-performance QD is good for the applicability of the

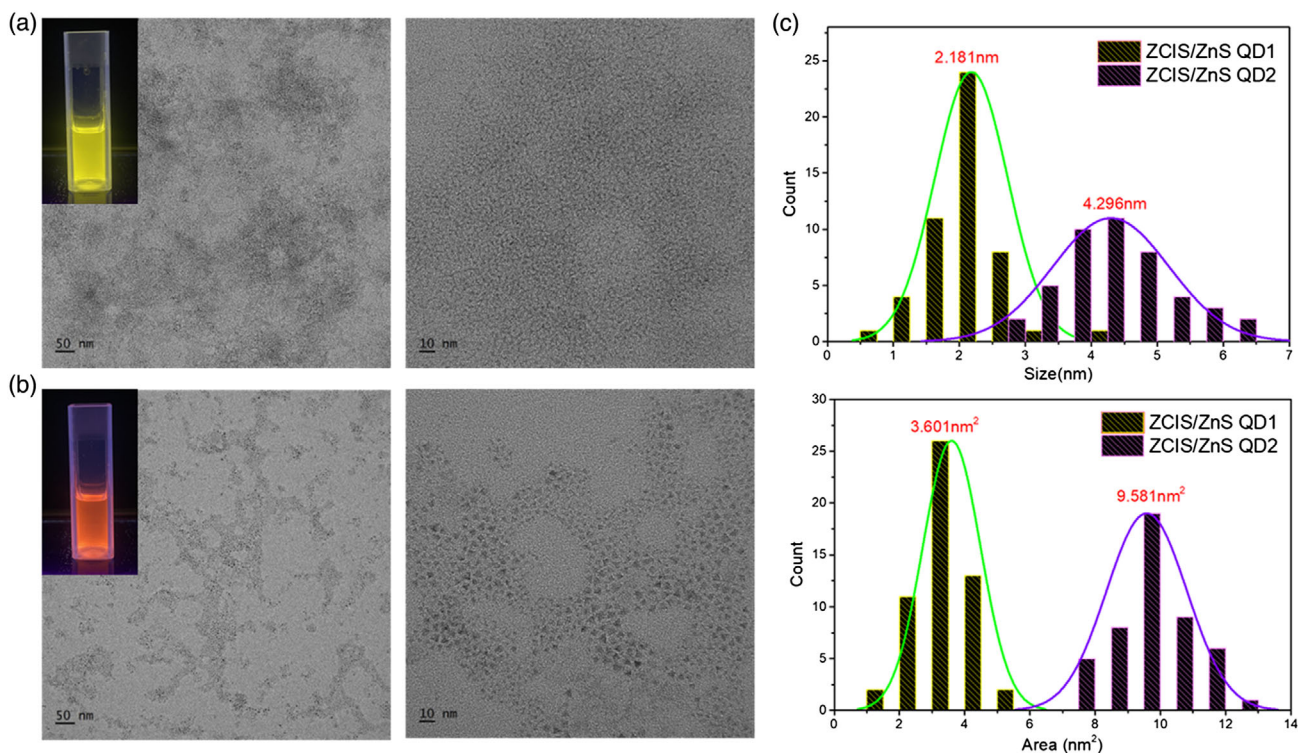


**Figure 2.** HR-TEM image of a) ZCIS/ZnS QD1, b) ZCIS/ZnS QD2, and c) size and area histogram of ZCIS/ZnS QDs.

device; therefore, ZQ1 was selected as the main ZQs. The selected ZQs are eco-friendly QD consisting of core/shell/ligand with 2.181 nm length and 3.601 nm<sup>2</sup> area on average. It can exist between thin D18-Cl film and PM6:BTP-eC9 (100 ≈ 120 nm) film, implementing a stable QDs hybrid system through the good organic compatibility of ligands in ZQs.

## 2.2. Optical Characteristics

**Figure 3** presents the photoluminescence (PL) and UV-vis spectra of active materials and ZQs. As shown in Figure 3a, the ZQs exhibit excitation in the UV region (<300 nm) with 550 nm emission. Figure 3b shows the PL change when D18-Cl is added as vol% to pristine ZQs solution. Pristine ZQs show an emission peak of 550 nm as shown in Figure 3a, whereas the addition of D18-Cl distinctly enhances the emission spectrum at 600–700 nm, which resembles the D18 series PL peak.<sup>[49,50]</sup> The increase in PL intensity of D18-Cl with a decrease of ZQs indicates the formation of an additional carrier through the FRET effect from the ZQs.<sup>[42,43]</sup>

The wide emission spectrum of D18-Cl + ZQs arises from the unbalanced binding energy due to the random core arrangement of ZCIS at the ZQs core.<sup>[31,32]</sup> Hence, the effective photons for D18-Cl and PM6, whose absorption ranges are well matched to the PL of ZQs, may increase through the light conversion action on the LAL. Figure 3c shows the PL of active mono and ternary films. D18-Cl, PM6, and BTP-eC9 mono films have PL peaks of 630, 740, and 850 nm, respectively. On the other hand, the ternary film shows significantly reduced intensity due to quenching by exciton dissociation through charge transfer at the D/A

interfaces. At this time, the ternary films containing ZQs tended to be more quenched in the active film, which means that exciton production and dissociation were promoted through the effective energy transfer of ZQs. More about PL and UV analysis for active solutions are provided in Figure S3, Supporting Information. Especially in Figure S3b, Supporting Information, as the amount of ZQs added to the active solution increases, the peaks indicating the donor and the acceptor all decrease due to the quenching effect of the active material. As consistent with previous reports on us, this study showed the FRET effect between the excited donor and ground-state acceptor.<sup>[43]</sup>

The trend of increased absorption due to the light-amplification effect of the ZQs was analyzed using a UV-vis spectrophotometer. Figure 3d,e presents the UV-vis spectra for the D18-Cl mono film and D18-Cl/PM6:BTP-eC9 blend film, respectively. When ZQs are added, the absorption intensities of all films' UV-vis spectra increase, indicating that the UV light was converted into the available effective light for the active materials through the ZQs. As previously described, the photon energy transfer effect of ZQs targeting the donor region interestingly causes the increasing trend to be more distinct for the absorption of the donor region (500–650 nm) than the acceptor region.

The light amplification through the FRET effect arises from the overlap between the emission domain of the ZQs and the absorption domain of the active layer. Here, the optical matching between the ZQs and the active system is critical; specifically, it is important that the absorption region of the active layer does not overlap with the excitation region of the ZQs but maximizes the overlap with the emission region of the ZQs. As shown in Figure 3f, the pristine ZQs are well matched with active materials

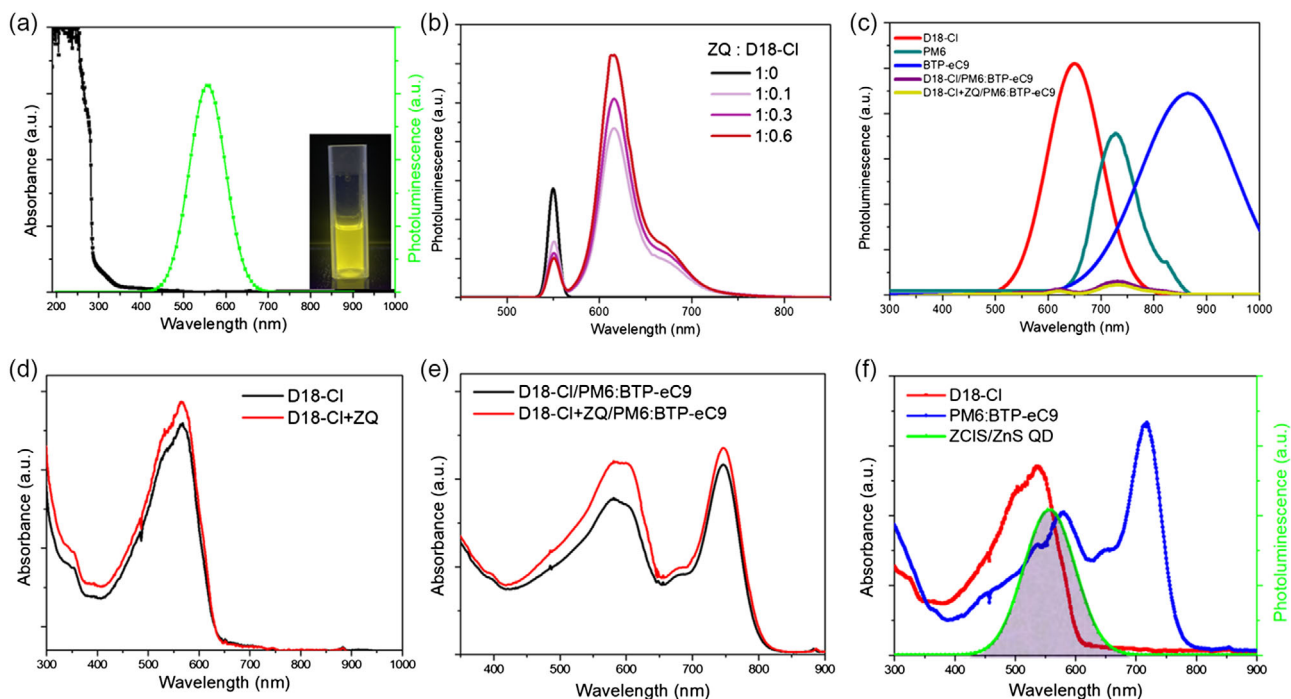


**Figure 3.** Photoluminescence of a) ZCIS/ZnS QDs, b) ZQs by introducing D18-Cl, c) mono or ternary active films, and absorbance of d) D18-Cl film, e) ternary active film by introducing ZQs, and f) overlap of ZQs PL and active absorbance.

by exciting with UV light and emitting across the absorption region for D18-Cl and PM6. The importance of this optical overlap is demonstrated in Figure S4, Supporting Information. The ZQ2, introduced at the top, shows an emission of 700 nm, which does not match well with the absorption region of the D18-Cl, PM6. For that reason, there are only increases in the donor peak according to the addition of D18-Cl and PM6 without reducing the ZQ2 emission peak.

Furthermore, we evaluated the optical properties of InP QD to prove the FRET effect. The InP QD has a similar emission wavelength and different quantum yield with ZQ1 (Figure S2, Supporting Information). The InP QD showed a PL peak of 550 nm that matches well with the D18-Cl and PM6 as well as ZQ1. In Figure S4, Supporting Information, the emission of InP QD decreased as a donor was added. The reason why the PL change is smaller than ZQ1 is that InP QD has a smaller quantum yield than ZQ1. This indicates that the additional light energy generated in InP QD caused FRET action in D18-Cl and PM6. As such, in the ZQs (ZQ1) that well overlapped with the donor and had great quantum yield, the effective light amplified through the QD allowed the donor to absorb more energy to generate additional electron charges. As a result, these FRET effects improved carrier transport in the active systems.<sup>[42,43]</sup>

### 2.3. Device Performance [1 sun]

In Figure 4a, three types of active system structures are schematically illustrated. Through these device structural changes, the effect of sub-D or LAL was compared. In the table below, OSCs composed of the LAL/BHJ active systems are expressed as ZQ-OSCs. The  $J-V$  curve of the manufactured device, EQE

spectrum, and photovoltaic performance are presented in Figure 4 and Table 2. While the power conversion efficiency (PCE) is 16.66% in the conventional PM6:BTP-eC9 system, it increases to 17.06% with the application of D18-Cl to the sub-D layer based on the clear increase in  $V_{OC}$  and the slight increase in  $J_{SC}$ . The low concentration of D18-Cl solution could decrease the current loss due to the energy barrier effect with deep HOMO levels and increases the carrier transport due to the electron withdrawal effect, improving  $V_{OC}$  (0.8287 eV  $\rightarrow$  0.8420 eV).

Meanwhile, ZQ-OSCs with LAL show a distinct increase in  $J_{SC}$  and yield the highest PCE of 17.60% through the improvement of overall characteristic factors. The light-amplification effect of the LAL as the main targets of ZQ-OSCs caused additional photons to be generated, increasing  $J_{SC}$ . Further, through the application of ZQs to the sub-D layer, the morphologies of the D18-Cl and PM6:BTP-eC9 active systems could be controlled, with positive effects on  $V_{OC}$  as well as FF.  $J-V$  curves reveal changes in  $V_{OC}$  and  $J_{SC}$  for the D18-Cl/PM6:BTP-eC9 device and ZQ-OSCs (Figure 4b). In addition, the EQE spectrum indicates that an improvement in EQE is mainly detected for the donor part (400–700 nm) of the ZQ-OSCs, which implies that the light amplification effect of the ZQs mainly occurs on the donor side. This result coincides with the optical property analysis in Figure 3, showing an increase in photon energy due to the effective photon amplification available by the donor.

### 2.4. Film Morphology Characteristics

Next, the morphological characteristics were analyzed for the polymer films according to ZQs doping through GIWAXS,

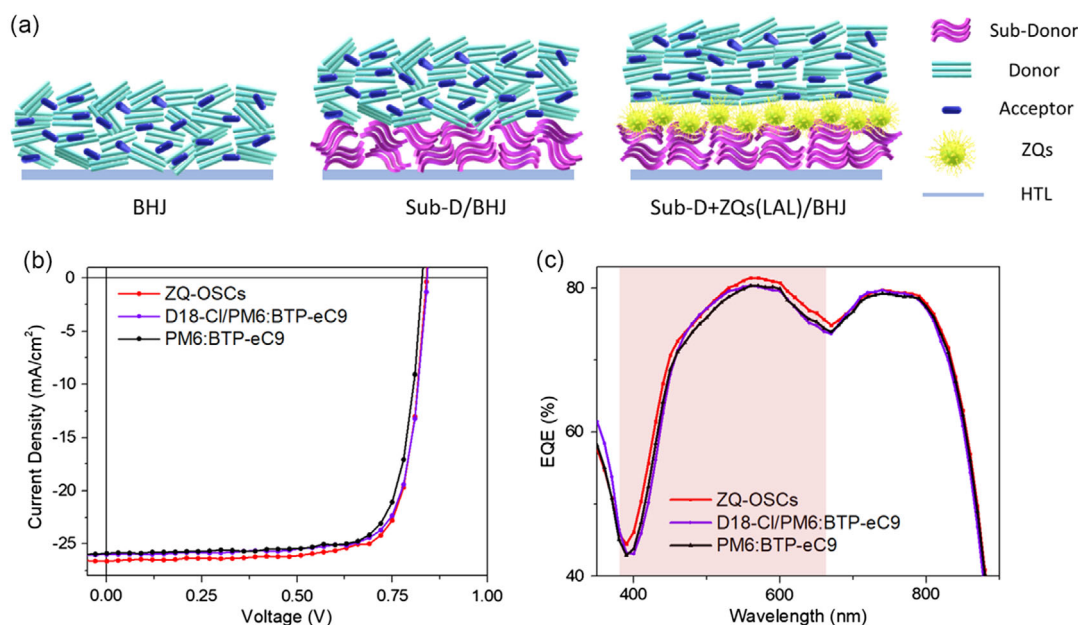


**Figure 4.** a) Active structures of three types of device, b)  $J$ - $V$  curve, and c) external quantum efficiency (EQE) spectrum of three types of device.

**Table 2.** Device performance in 1 sun (A.M. 1.5G).

Device	$J_{sc}$ [ $\text{mA cm}^{-2}$ ]	$J_{sc}^{cal}$ [ $\text{mA cm}^{-2}$ ]	$V_{oc}$ [V]	FF [%]	PCE [%]
ZQ-OSCs	26.36	24.67	0.8437	79.16	17.60
D18-Cl/PM6:BTP-eC9	25.99	24.21	0.8420	77.95	17.06
PM6:BTP-eC9	25.89	24.34	0.8287	77.67	16.66

transmission electron microscopy (TEM), and AFM. The polymer films are depicted for D18-Cl (Figure 5a), D18-Cl + ZQs (Figure 5b), D18-Cl/PM6:BTP-eC9 (Figure 5c), and D18-Cl + ZQs/PM6:BTP-eC9 (Figure 5d). The pristine D18-Cl film (Figure 5a) has OOP(010), IP(100), and (200) peaks, revealing a mixed orientation with the presence of both face-on and edge-on structures, of which the face-on structure appears to be dominant.<sup>[51]</sup> The pristine D18-Cl film coated with PM6:BTP-eC9 (Figure 5c) has strong OOP(010) and IP(100) peaks to display a clear face-on structure. This finding indicates the main orientation of the PM6:BTP-eC9 BHJ film.<sup>[52]</sup>

Meanwhile, D18-Cl + ZQs (Figure 5b) and D18-Cl + ZQs/BHJ (Figure 5d) films with the addition of ZQs lead to an increase in peak intensity across both the OOP(010) and IP(100) peaks. This result indicates the interaction between the hydrophobic ligand present on the ZQs shell and the active materials, causing  $\pi$ - $\pi$  stacking and further strengthening the lamellar stacking. Such increased vertical orientation due to the characteristics of OSCs structural change leads to enhanced effects on charge transport.<sup>[53,54]</sup> However, when ZQs are directly applied to the PM6:BTP-eC9 and not to the sub-D layer, the intensity of the vertical orientation decreases, as shown in Figure S5a, Supporting Information. The direct application of the ZQs in the PM6:BTP-eC9 produces film morphology degradation. This problem can be resolved through the application of ZQs to the sub-D layer. The line-cut profiles in-plane and out-of-plane upon the addition of ZQs to D18-Cl and D18-Cl/PM6:BTP-eC9 film, respectively, are presented in Figure S5b, Supporting Information. A clear increase in intensity is confirmed for D18-Cl + ZQs, whereas D18-Cl + ZQs/PM6:BTP-eC9 shows a slight improvement.

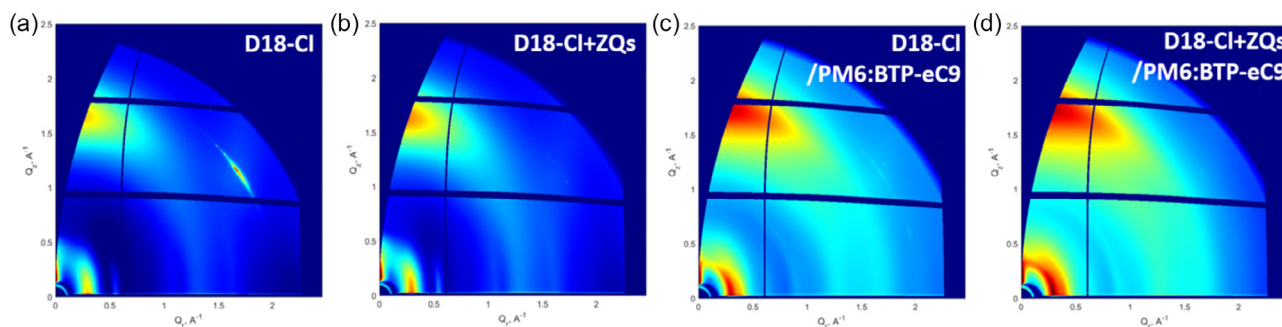


**Figure 5.** GIWAXS images a,b) D18-Cl(w/o or w ZQs) films, c,d) D18-Cl(w/o or w ZQs)/PM6:BTP-eC9 films.

The distances according to the molecular stacking crystallites and the orientation were calculated for the four films, as presented in Table 3. The calculated crystallite coherence lengths (CCLs) show that, with ZQs addition, the level of lamellar stacking increased by 0.528 and 0.096 nm, respectively, for D18-Cl and D18-Cl/PM6:BTP-eC9 films at IP(100). At OOP(010), indicating  $\pi$ - $\pi$  stacking, only the D18-Cl + ZQs film shows an increase, by 0.073 nm, whereas no change is observed for the D18-Cl + ZQs/PM6:BTP-eC9 film. The increase in CCL indicates higher crystallinity and more uniform film formation. In contrast, the d-spacing shows a decreasing trend for the D18-Cl + ZQs and D18-Cl + ZQs/PM6:BTP-eC9 films. As the d-spacing indicates the distance between the crystals by their orientation, the shorter distances imply a more densely aligned polymer film.<sup>[55,56]</sup> The numerical value in d-spacing with ZQs application tends to be higher change for the D18-Cl + ZQs mono film than for the D18-Cl + ZQs/PM6:BTP-eC9 blend film, coinciding with the previous GIWAXS results to suggest a higher level of compatibility with the application of ZQs to D18-Cl. Ultimately, ZQs addition improves the crystallinity of the polymer groups and generates a uniform film by the molecular alignment. This behavior leads to effective charge transport as the bond length between the crystals decreases.

Figure 6 shows the TEM results for the ZQs-modified film surface structure. In Figure 6b, the film with ZQs application displays a nanocrystal structure with a clear branched pattern. Moreover, a distinct branched pattern was observed in Figure 6d, in which D18-Cl + ZQs was laid as a sublayer.<sup>[57]</sup> The analysis thus verifies the phase separation of the films based on the hydrophobic ZQs ligand, which generates the interaction with active materials. Figure 7 and Table 4 present the respective AFM images and the values of the root mean square (RMS),  $R_{\text{mean}}$ , and  $R_q$  for the films, where RMS indicates the surface roughness,  $R_{\text{mean}}$  is the surface potential, and  $R_q$  is the mean

difference in the surface potential. An increase in the surface potential for a polymer film implies an increase in stability based on the cohesion degradation through Brownian motion. In addition, as the difference in surface potential reflects the voltage, a larger difference leads to a higher level of charge transport within the cell.<sup>[58]</sup> In a hybrid film combining ZQs with D18-Cl, the RMS roughness was shown to increase from 0.7255 to 0.7736 nm due to the size and electrical properties of the inorganic ZQs.  $R_{\text{mean}}$  and  $R_q$  also increase by 4.375 and 0.347 mV, respectively. In contrast, no significant change in roughness is observed for the D18-Cl + ZQs/PM6:BTP-eC9 system, with  $R_{\text{mean}}$  and  $R_q$  decreased.

The nonuniformity of the thin film according to the particle size of ZQs can be solved by coating BHJ on the LAL, and ZQs can be effectively positioned in the ternary active system. In addition, as the ZQ ligand contributes to the control of the interface between the sub-D layer and BHJ layer, the surface uniformity increases compared to that of the pristine D18-Cl/PM6:BTP-eC9 film.<sup>[59,60]</sup> Through this morphological analysis, it can be verified that the active structure in which the LAL and BHJ layers are stacked using the LBL coating method placed ZQs at the optimal position as shown in Figure 3a and implemented a multilayer thin film that is good for carrier transfer.

Electrons move from low to high surface potential. Here, for the conventional device, because the surface potential with the ETL increases as the surface potential with the active layer decreases, a positive effect is exerted on the carrier transfer.<sup>[42,43]</sup> Ultimately, the D18-Cl + ZQs/PM6:BTP-eC9 film acquires a reduced surface potential due to the ZQs interaction at the junction of two layers, forming a more effective electric field. These interface changes lead to a good electron withdrawal effect of the D18-Cl surface in addition to the improved surface contact and charge transport, with positive effects on the characteristics of  $V_{\text{OC}}$  and FF.

**Table 3.** CCL, d-spacing calculation through GIWAXS data.

Formed films	IP(100)_lamellar stacking			OOP(010)_ $\pi$ - $\pi$ stacking		
	q [ $\text{\AA}^{-1}$ ]	CCL [nm]	$d_{100}$ [nm]	q [ $\text{\AA}^{-1}$ ]	CCL [nm]	$d_{010}$ [nm]
D18-Cl	0.299	5.802	0.1887	1.649	1.820	1.036
D18-Cl + ZQs	0.296	6.330	0.1862	1.627	1.893	1.022
D18-Cl/PM6:BTP-eC9	0.311	5.944	0.1953	1.726	2.094	1.085
D18-Cl + ZQs/PM6:BTP-eC9	0.311	6.040	0.1946	1.708	2.094	1.073

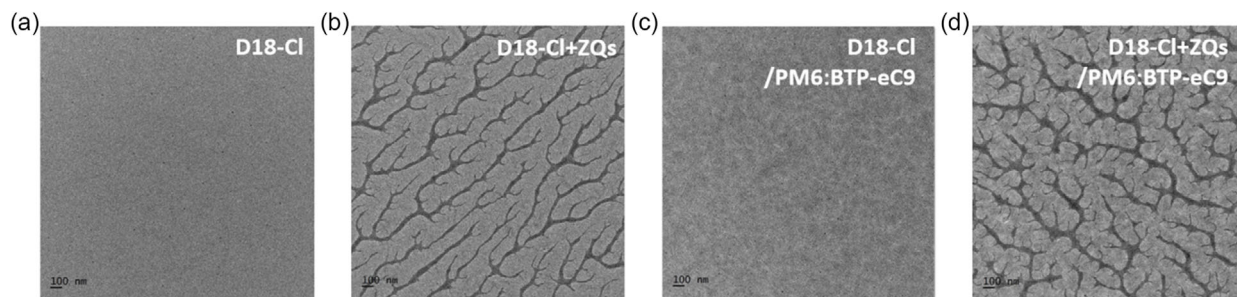


**Figure 6.** HR-TEM images of a,b) D18-Cl(w/o or w ZQs) films, c,d) D18-Cl(w/o or w ZQs)/PM6:BTP-eC9 films.

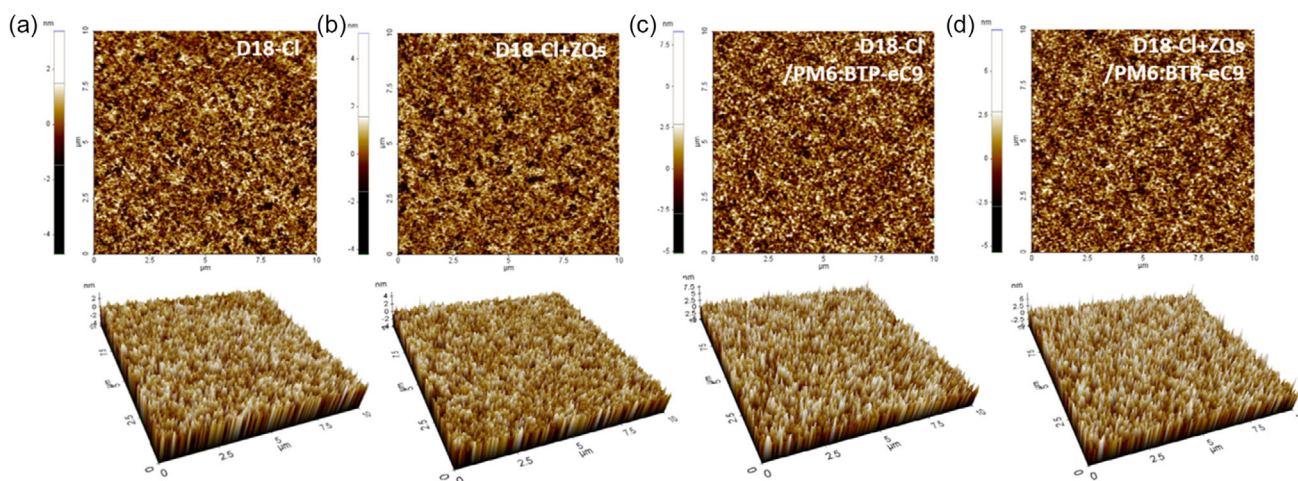


**Figure 7.** AFM images of a,b) D18-Cl(w/o or w ZQs) films, c,d) D18-Cl(w/o or w ZQs)/PM6:BTP-eC9 films.

**Table 4.** Films RMS roughness,  $R_{\text{mean}}$ , and  $R_q$  calculated by AFM data.

Formed films	RMS [nm]	$R_{\text{mean}}$ [mV]	$R_q$ [mV]
D18-Cl	0.7255	682.527	5.117
D18-Cl + ZQs	0.7736	686.902	5.464
D18-Cl/PM6:BTP-eC9	1.341	664.057	20.895
D18-Cl + ZQs/PM6:BTP-eC9	1.340	663.697	20.182

## 2.5. Surface and Molecular Characteristics

Figure 8 shows the XPS analysis results according to the ZQs distribution within the film. Figure 7a–c provides the respective spectrum for the N 1s, S 2p, and Zn 2p binding energies on the pristine D18-Cl film and D18-Cl + ZQ film surfaces. No significant change in binding energy is detected for the main elements, N 1s (Figure 7a) and S 2p (Figure 7b), of D18-Cl, with intensities that are almost identical to one another. Figure 8c presents the binding energies at 1022.51 and 1045.34 eV for the Zn element of the shell in ZQs distributed across the film surface.<sup>[61,62]</sup> It indicates an adequate distribution of ZQs on the surface. Figure 8d–f depicts the surface analysis results for the blend films coated with D18-Cl/PM6:BTP-eC9 and D18-Cl + ZQ/PM6:BTP-eC9. Interestingly, no Zn is evident in Figure 8g. It suggests that the thickness of the BHJ film prevented ZQs exposure on the surface, at once the ZQs were securely fixed between the sub-D layer and the BHJ layer.

The ZQs-added films in Figure 8d–g showed an obvious decrease in intensity with a slight upshift at both N 1s, S 2p, and O 1s peak. Notably, the trend of decreasing intensity is more evident for the multilayers (Figure 8d–f) than for the monolayers (Figure 8a–c), with the most distinct change observed for O 1s (Figure 8f). The decrease in the O 1s peak for the films with ZQ indicates additional second-order bonds were created due to the interaction with the ZQs ligand between D18-Cl and the PM6:BTP-eC9 hybrid system.<sup>[63,64]</sup> Such surface characteristics can be confirmed by the EDS mapping results in Figure S6, Supporting Information. The Zn element that is not evident for

the pristine D18-Cl film (Figure S2a, Supporting Information) is detected in a uniform distribution for the D18-Cl + ZQs film (Figure S2b, Supporting Information). The increased portions of Zn and S, the main elements in the ZQs, also clearly reduce the distribution intensities of the main elements (C, N, Cl, and O) of the active polymer, which matches the previous XPS analysis results. The results, alongside the previously described AFM analysis, showed that the ZQs were effectively added through the LAL/BHJ structure and a uniform multilayer thin film was formed.

## 2.6. Electric and Electronic Characteristics

Analyses of the carrier generation and carrier recombination on the optoelectronic semiconductor are essential to identifying the drive pattern of the device. In this study, the analyses were performed for three cases: PM6:BTP-eC9-based OSCs, D18-Cl/PM6:BTP-eC9-based OSCs, and ZQ-OSCs with LAL. Figure 9a,b shows the relationships between the current density and voltage according to the light intensity of each device, and the calculated values obtained from the plot are listed in Table S2, Supporting Information.

Through the light intensity analysis, the exciton dissociation and charge collection can be determined. The  $\alpha$  in the  $P_{\text{light}}$  versus  $J_{\text{SC}}$  plot indicates the level of bimolecular recombination, where a device with a value close to 1 indicates an ideal device with adequate suppression of bimolecular recombination. Meanwhile,  $KT/q$  in the  $P_{\text{light}}$  versus  $V_{\text{OC}}$  plot indicates the dominant recombination type between bimolecular recombination and trap-assisted recombination. As  $KT/q$  approaches 1, the bimolecular recombination is dominant, and as it approaches 2, the trap-assisted recombination is dominant.<sup>[65,66]</sup>

The slope  $\alpha$  in the  $P_{\text{light}}$  versus  $J_{\text{SC}}$  plot is 1.0298, 1.0338, and 1.0329 for ZQ-OSCs, D18-Cl/PM6:BTP-eC9, and PM6:BTP-eC9, respectively. The addition of a D18-Cl monofilm without ZQs increased bimolecular recombination, compared to the case of PM6:BTP-eC9, but the ZQ-OSCs exhibit the  $\alpha$  value closest to 1 of the three devices, implying that they most effectively inhibited binary recombination. In addition, the  $KT/q$  of the device based on the maximum and minimum impressed voltage values



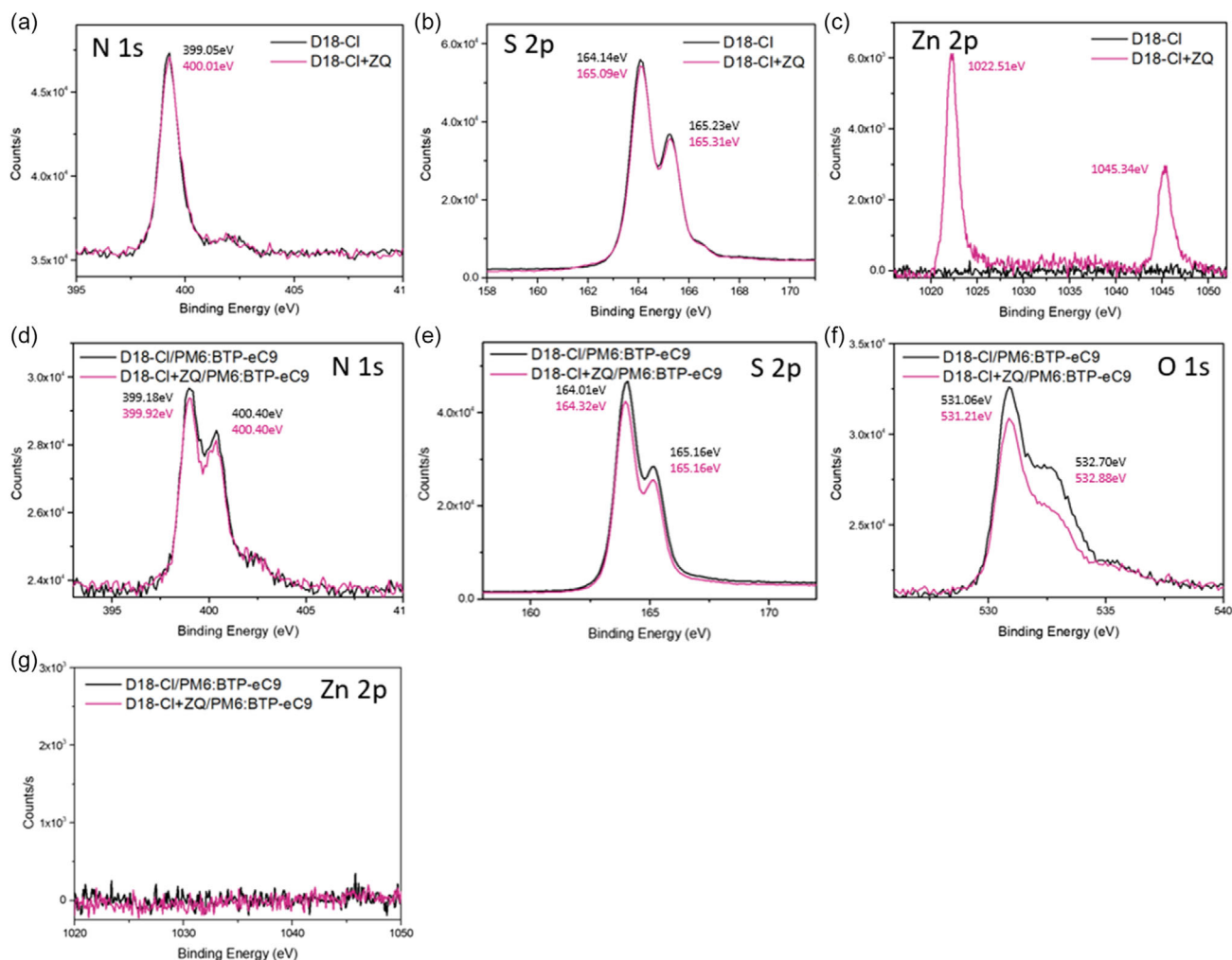


**Figure 8.** X-ray photoelectron spectroscopy (XPS) data a–c) D18-Cl(w/o or w ZQs) films, d–g) D18-Cl(w/o or w ZQs)/PM6:BTP-eC9 films.

is 1.0807, 1.0868, and 1.0753 for the ZQ-OSCs, D18-Cl/PM6:BTP-eC9, and PM6:BTP-eC9, respectively. In all three device driving patterns, trap-assisted recombination was dominant at low input voltage, and bimolecular recombination was dominant at high input voltage. The D18-Cl/PM6:BTP-eC9 shows an increase in trap-assisted recombination compared to PM6:BTP-eC9, whereas the ZQ-OSCs effectively suppress. These results match with the recombination pattern obtained based on  $P_{\text{light}}$  versus  $J_{\text{SC}}$ .

The  $J_{\text{ph}}$  versus  $V_{\text{eff}}$  plot in Figure 9c is provided for charge collection analysis according to exciton generation. All three devices showed saturation curves in the form of root functions according to the formation of the space charge layer for  $V_{\text{eff}}$ , which increases up to 1 V. The PM6:BTP-eC9 and D18-Cl/PM6:BTP-eC9 are saturated at  $V_{\text{eff}} < 0.4$  V, and the ZQ-OSCs saturated at  $V_{\text{eff}} < 0.3$  V. The ZQ-OSCs show a low saturated  $V_{\text{eff}}$  value and higher exciton collection efficiency, and this aspect can be attributed to the decrease in leakage current based on the morphological change induced by LAL.<sup>[67–69]</sup> To verify the effect, the dark current analysis was performed, and the results are presented in Figure 9d. The dark current density of the

ZQ-OSCs under the reverse bias condition is markedly lower than that observed for the other two devices. The main cause of the decrease in the reverse leakage current is the significant improvement in shunt resistance to  $2157.8 \Omega \text{ cm}^2$  with ZQs application.<sup>[65]</sup> The altered film morphology as a result of LAL introduction promotes the formation of an additional carrier transport channel within the device to reduce the dark current density. These results prove the positive effect of ZQs on exciton dissociation and charge collection, as shown in the photocurrent density analysis (Figure 10).

## 2.7. Additional Performance of ZQ-OSCs

The light amplification effect of LAL introduced in ZQ-OSCs can provide significant advantages in low-light environments with fewer effective photons. Thus, we measure the three types of OSCs through LED lamp to observe the performance change under indoor light when the sub-D layer or LAL was introduced. Figure 10 presents the  $J$ - $V$  curve for each device, as measured in an indoor system. The incident light was measured at

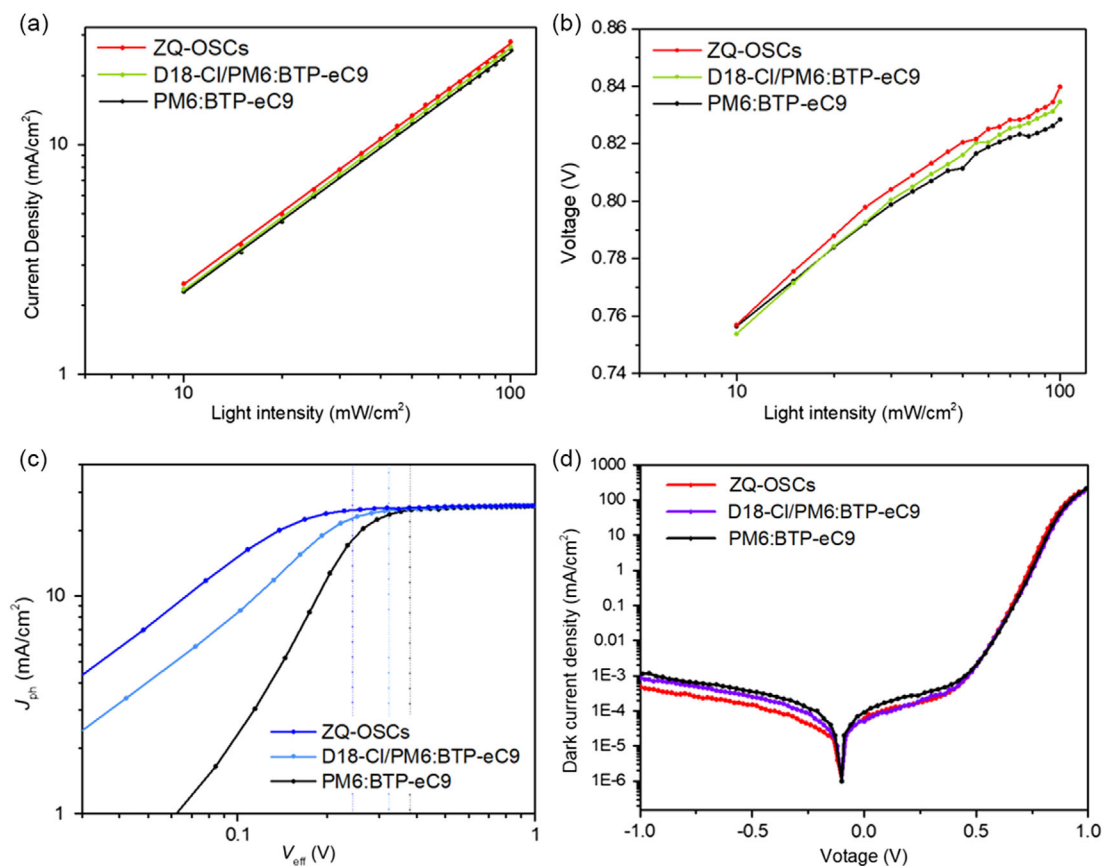


**Figure 9.** a)  $P_{\text{light}}$  versus  $J_{\text{SC}}$  plot, b)  $P_{\text{light}}$  versus  $V_{\text{OC}}$  plot, c)  $J_{\text{ph}}$ , photocurrent density versus  $V_{\text{eff}}$ , effective voltage plot, d) dark current density.

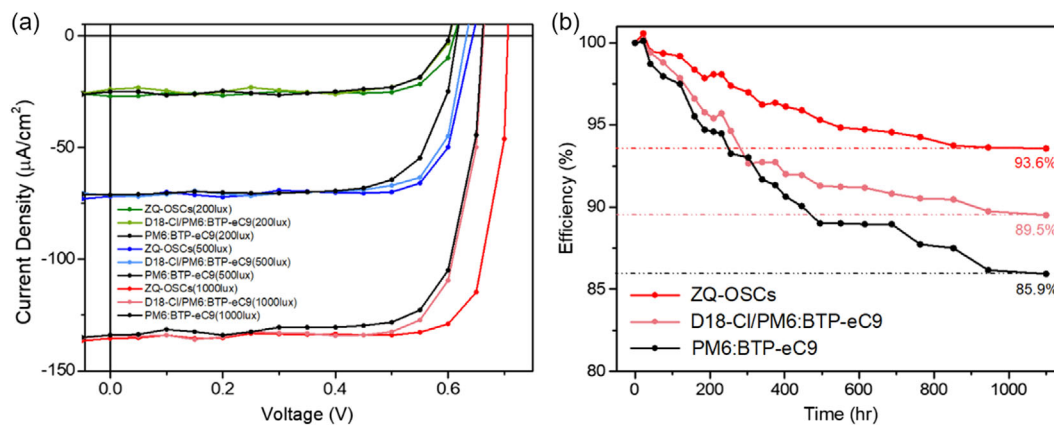


**Figure 10.** a)  $J$ - $V$  curve in the indoor system, b) device stability in the glovebox ( $N_2$  environment).

3000 K, under 200, 500, and 1000 lux illumination. The results are presented in Table 5. For the ZQ-OSCs,  $J_{\text{SC}}$  increases under all three lux conditions, especially at 200 lux. Moreover, ZQ-OSCs and D18-Cl/PM6:BTP-eC9 both exhibit notable improvements of  $V_{\text{OC}}$  and FF in indoor light as in the case of 1 sun. After optimization, the ZQ-OSCs finally achieved  $\text{PCE} = 23.39\%$  with  $J_{\text{SC}} = 135.5 \mu\text{A cm}^{-2}$  and  $P_{\text{out}} = 77.4258 \mu\text{W cm}^{-2}$  at 3000 K and 1000 lux.

The ZQ-OSCs also showed outstanding device stability compared to other devices, and follow-up monitoring for 1100 h or more revealed that the PCE could be maintained above 93% (Figure 10). Through these results, it was confirmed that the morphological surface change by LAL had a positive effect on device stability. The findings suggest that the optical, morphological, and electronic effects of LAL could be maintained even in low-light environments, implying effective

**Table 5.** Device performance in indoor (3000 K).

Indoor [3000 K]	Device	$J_{SC}$ [ $\mu A\ cm^{-2}$ ]	$V_{OC}$ [V]	FF [%]	PCE [%]	$P_{out}$ [ $\mu W\ cm^{-2}$ ]
1000 lux	ZQ-OSCs	135.5	0.7062	80.91	23.39	77.43
	D18-Cl/PM6:BTP-eC9	134	0.6630	78.81	21.15	70.01
	PM6:BTP-eC9	134	0.6612	76.23	20.40	67.53
500 lux	ZQ-OSCs	72.0	0.6644	78.28	21.74	36.31
	D18-Cl/PM6:BTP-eC9	71.5	0.6329	77.20	20.92	34.94
	PM6:BTP-eC9	71.25	0.6159	73.52	19.32	32.26
200 lux	ZQ-OSCs	27.1	0.6114	76.37	19.47	12.65
	D18-Cl/PM6:BTP-eC9	24.05	0.6031	79.29	17.70	11.5
	PM6:BTP-eC9	25.05	0.6022	76.91	17.85	11.6

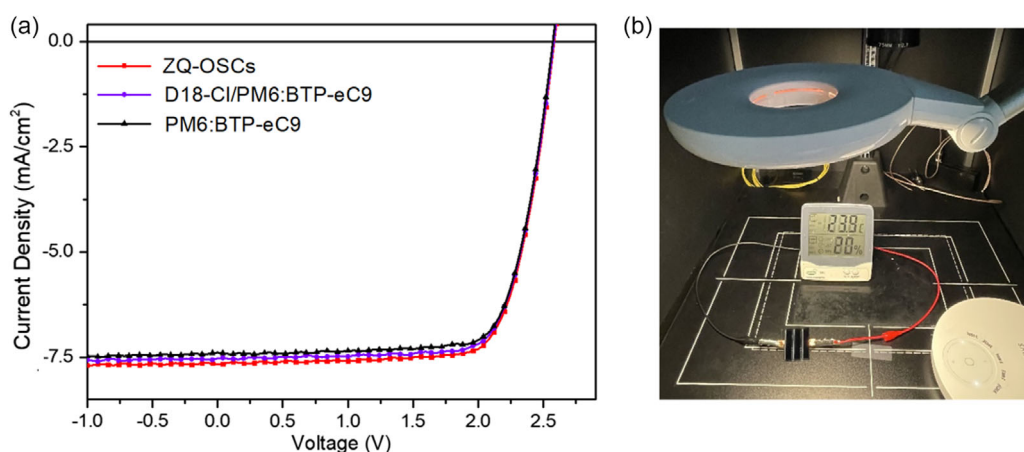


**Figure 11.** a)  $J$ - $V$  curve of three types module ( $4.7\ cm^2$ ), b) module driven at low light environment (3000 K LED lamp).

interaction and compatibility between the active materials and the ZQs.

Next, we manufactured an OSCs module to confirm the large-area applicability of LAL. The  $J$ - $V$  curve and device performance of the three type modules are shown in **Figure 11** and **Table 6**. Although FF decreased slightly during the large area process, overall performances were improved, such as unit cells. This is a result of the positive effects of the light amplification and molecular interaction by ZQs, and it showed excellent efficiency of 14.72% in the ZQ-OSCs module. Figure 11b displays the driving process of the thermohygrometer through the ZQ-OSCs module under the 3000 K LED lamp. As a result, since ZQ-OSCs exhibit good applicability in various environments, it is suggested that ZQ-OSCs containing QDs-hybrid LAL are an effective device strategy.

**Table 6.** OSCs-module ( $4.7\ cm^2$ ) performance in 1 sun (A.M. 1.5G).

Device	$J_{SC}$ [ $mA\ cm^{-2}$ ]	$V_{OC}$ [V]	FF [%]	PCE [%]
ZQ-OSCs	7.66	2.583	74.36	14.72
D18-Cl/PM6:BTP-eC9	7.525	2.58	74.79	14.52
PM6:BTP-eC9	7.383	2.573	75.66	14.37

### 3. Conclusion

The strategy of introducing LAL (composed of D18-Cl + ZQs) as a sub-layer of OSCs not only increased the optoelectronic properties but also had a positive effect on stability. The QDs-hybrid system using nontoxic ZQs exhibited outstanding compatibility with D18-Cl and PM6:BTP-eC9 as the active layer. In the optimized ternary structure stacked with LAL and BHJ through the LBL coating, effective light amplification occurred and the morphology of the ternary active system was improved.

Particularly, additional carrier production through the emission effect of ZQs core increased the effective light energy of active, and the molecular interaction of ZQs ligand enhanced interfacial contact of the multiactive system. As a result, the ZQ-OSCs could achieve 17.60% PCE ( $J_{SC} = 26.36\ mA\ cm^{-2}$ ,  $V_{OC} = 0.8437\ V$ , and  $FF = 79.16\%$ ) with outstanding stability to maintain 93.6% after 1100 h. Furthermore, the ZQ-OSCs achieve 23.39% PCE with  $77.4258\ \mu W/cm^2$  power at indoor light (3000 K, 1000 lux) and the ZQ-OSCs module showed the best efficiency of 14.72%, this performance confirmed that device structure with LAL has great applicability for low-light environments and large-area applications. This study provides a high-efficiency and high-stability OSCs strategy based on the

inorganic/organic interaction of QDs-hybrid system and suggests that QD-OSCs have excellent potential for future solar energy technology.

## Supporting Information

Supporting Information is available from the Wiley Online Library or from the author.

## Acknowledgements

This paper was supported by the National Research Foundation of Korea (NRF) (grant no. 2020R1A2C2010916), Ministry of Trade, Industry and Energy (MOTIE), and Korea Institute for Advancement of Technology (KIAT) through the International Cooperative R&D program (Project no. P0019184) and Korea Institute of Energy Technology Evaluation and Planning (KETEP) and the Ministry of Trade, Industry and Energy (MOTIE) of the Republic of Korea (grant no. 20228A10100040).

## Conflict of Interest

The authors declare no conflict of interest.

## Data Availability Statement

The data that support the findings of this study are available from the corresponding author upon reasonable request.

## Keywords

eco-friendly QDs, effective ternary active structures, great applicability, high-performance with high-stability, ligand interactions, light-amplification-layer, QDs-hybrid

Received: February 20, 2023

Published online:

- [1] M. Riede, D. Spoltore, K. Leo, *Adv. Energy Mater.* **2021**, *11*, 2002653.
- [2] D. Luo, W. Jang, D. D. Babu, M. S. Kim, D. H. Wang, A. K. K. Kyaw, *J. Mater. Chem. A Mater.* **2022**, *10*, 3255.
- [3] L. Duan, B. Hoex, A. Uddin, *Sol. RRL* **2021**, *5*, 2100041.
- [4] D. Wang, H. Liu, Y. Li, G. Zhou, L. Zhan, H. Zhu, X. Lu, H. Chen, C. Z. Li, *Joule* **2021**, *5*, 945.
- [5] C. Liu, C. Xiao, C. Xie, W. Li, *Nano Energy* **2021**, *89*, 106399.
- [6] Y. Cui, L. Hong, J. Hou, *ACS Appl. Mater. Interfaces* **2020**, *12*, 38815.
- [7] J. Wang, M. Zhang, J. Lin, Z. Zheng, L. Zhu, P. Bi, H. Liang, X. Guo, J. Wu, Y. Wang, L. Yu, J. Li, J. Lv, X. Liu, F. Liu, J. Hou, Y. Li, *Energy Environ. Sci.* **2022**, *15*, 1585.
- [8] Z. Zheng, J. Wang, P. Bi, J. Ren, Y. Wang, Y. Yang, X. Liu, S. Zhang, J. Hou, *Joule* **2022**, *6*, 171.
- [9] R. Peng, T. Yan, J. Chen, S. Yang, Z. Ge, M. Wang, *Adv. Electron. Mater.* **2020**, *6*, 1901245.
- [10] Y. Wang, B. Jia, J. Wang, P. Xue, Y. Xiao, T. Li, J. Wang, H. Lu, Z. Tang, X. Lu, F. Huang, X. Zhan, *Adv. Mater.* **2020**, *32*, 2002066.
- [11] L. Yan, Y. Yang, C. Q. Ma, X. Liu, H. Wang, B. Xu, *Carbon N. Y.* **2016**, *109*, 598.
- [12] S. W. Baek, S. Jun, B. Kim, A. H. Proppe, O. Ouellette, O. Voznyy, C. Kim, J. Kim, G. Walters, J. H. Song, S. Jeong, H. R. Byun, M. S. Jeong, S. Hoogland, F. P. García de Arquer, S. O. Kelley, J. Y. Lee, E. H. Sargent, *Nat. Energy* **2019**, *4*, 969.
- [13] Y. Tao, H. Liu, D. Wang, F. Zhao, Z. Chen, H. Zhu, H. Chen, C. Z. Li, *InfoMat* **2022**, *4*, e12276.
- [14] W. Miao, C. Guo, D. Li, T. Li, P. Wang, Y. Yang, D. Liu, T. Wang, *Sol. RRL* **2021**, *5*, 2100499.
- [15] J. S. Shaikh, N. S. Shaikh, S. S. Mali, J. v. Patil, S. A. Beknalkar, A. P. Patil, N. L. Tarwal, P. Kanjanaboos, C. K. Hong, P. S. Patil, *ChemSusChem* **2019**, *12*, 4724.
- [16] J. Kim, S. Song, Y.-H. Kim, S. K. Park, *Small Struct.* **2021**, *2*, 2000024.
- [17] M. Chen, J. Wang, F. Yin, Z. Du, L. A. Belfiore, J. Tang, *J. Mater. Chem. A Mater.* **2021**, *9*, 4505.
- [18] X. Li, H. Yang, X. Du, H. Lin, G. Yang, C. Zheng, S. Tao, *Chem. Eng. J.* **2023**, *452*, 139496.
- [19] J. Wang, S. Wen, J. Hu, J. Han, C. Yang, J. Li, X. Bao, S. Yan, *Chem. Eng. J.* **2023**, *452*, 139462.
- [20] J. Farinhas, S. F. H. Correia, L. Fu, A. M. P. Botas, P. S. André, R. A. S. Ferreira, A. Charas, *Front. Nanotechnol.* **2021**, *3*, 635929.
- [21] Y. Wang, Y. Liu, G. Xie, J. Chen, P. Li, Y. Zhang, H. Li, *ACS Appl. Mater. Interfaces* **2022**, *14*, 5951.
- [22] L. Hong, H. Yao, Y. Cui, P. Bi, T. Zhang, Y. Cheng, Y. Zu, J. Qin, R. Yu, Z. Ge, J. Hou, *Adv. Mater.* **2021**, *33*, 2103091.
- [23] G. P. Forcade, A. Ritou, P. St-Pierre, O. Dellea, M. Volatier, A. Jaouad, C. E. Valdivia, K. Hinzer, M. Darnon, *Prog. Photovoltaics Res. Appl.* **2022**, *30*, 132.
- [24] D. Lübke, P. Hartnagel, J. Angona, T. Kirchartz, *Adv. Energy Mater.* **2021**, *11*, 2101474.
- [25] L. Xie, W. Song, J. Ge, B. Tang, X. Zhang, T. Wu, Z. Ge, *Nano Energy* **2021**, *82*, 105770.
- [26] Y. Ding, M. Young, Y. Zhao, C. Traverse, A. Benard, R. R. Lunt, *Sol. Energy Mater. Sol. Cells* **2015**, *132*, 523.
- [27] J. Gulomov, R. Aliev, A. Mirzaalimov, N. Mirzaalimov, J. Kakhkhorov, B. Rashidov, S. Temirov, *Int. J. Renewable Energy Dev.* **2021**, *10*, 731.
- [28] R. Datt, S. Bishnoi, H. K. H. Lee, S. Arya, S. Gupta, V. Gupta, W. C. Tsoi, *Aggregate* **2022**, *3*, e185.
- [29] H. Zhao, F. Rosei, *Chem* **2017**, *3*, 229.
- [30] M. Liu, N. Yazdani, M. Yarema, M. Jansen, V. Wood, E. H. Sargent, *Nat. Electron.* **2021**, *4*, 548.
- [31] X. Bai, F. Purcell-Milton, Y. K. Gun'ko, *Nanomaterials* **2019**, *9*, 85.
- [32] Z. Long, W. Zhang, J. Tian, G. Chen, Y. Liu, R. Liu, *Inorg. Chem. Front.* **2021**, *8*, 880.
- [33] H. S. Shim, M. Ko, S. Jeong, S. Y. Shin, S. M. Park, Y. R. Do, J. K. Song, *J. Phys. Chem. C* **2021**, *125*, 9965.
- [34] F. W. Eagle, N. Park, M. Cash, B. M. Cossairt, *ACS Energy Lett.* **2021**, *6*, 977.
- [35] I. A. Mir, K. Das, T. Akhter, R. Ranjan, R. Patel, H. B. Bohidar, *RSC Adv.* **2018**, *8*, 30589.
- [36] M. Ko, H. C. Yoon, H. Yoo, J. H. Oh, H. Yang, Y. R. Do, *Adv. Funct. Mater.* **2017**, *27*, 1602638.
- [37] W. Guo, N. Chen, Y. Tu, C. Dong, B. Zhang, C. Hu, J. Chang, *Theranostics* **2013**, *3*, 99.
- [38] C. Xia, J. D. Meeldijk, H. C. Gerritsen, C. de Mello Donega, *Chem. Mater.* **2017**, *29*, 4940.
- [39] N. Y. Doumon, L. Yang, F. Rosei, *Nano Energy* **2022**, *94*, 106915.
- [40] X. K. Yang, J. W. Qiao, Z. H. Chen, Z. C. Wen, H. Yin, X. T. Hao, *J. Phys. D Appl. Phys.* **2021**, *54*, 115504.
- [41] D. H. Shin, C. W. Jang, J. S. Ko, S. H. Choi, *Appl. Surf. Sci.* **2021**, *538*, 148155.
- [42] Y. W. Han, C. H. Jung, H. S. Lee, S. J. Jeon, D. K. Moon, *ACS Appl. Mater. Interfaces* **2020**, *12*, 38470.
- [43] Y. W. Han, S. J. Jeon, J. Y. Choi, J. H. Kim, D. K. Moon, *Sol. RRL* **2018**, *2*, 1800077.

- [44] M. Guan, W. Tao, L. Xu, Y. Qin, J. Zhang, S. Tan, M. Huang, B. Zhao, *J. Mater. Chem. A Mater.* **2022**, *10*, 9746.
- [45] G. Zhang, K. Zhang, Q. Yin, X. F. Jiang, Z. Wang, J. Xin, W. Ma, H. Yan, F. Huang, Y. Cao, *J. Am. Chem. Soc.* **2017**, *139*, 2387.
- [46] J. Qin, L. Zhang, C. Zuo, Z. Xiao, Y. Yuan, S. Yang, F. Hao, M. Cheng, K. Sun, Q. Bao, Z. Bin, Z. Jin, L. Ding, *J. Semicond.* **2021**, *42*, 010501.
- [47] A. Goktas, E. Aslan, F. Arslan, A. Kilic, *Opt. Mater.* **2022**, *133*, 112984.
- [48] A. Tumbul, F. Aslan, A. Goktas, M. Z. Zarbali, A. Kilic, *Mater. Chem. Phys.* **2021**, *258*, 123997.
- [49] J. Hofinger, C. Putz, F. Mayr, K. Gugujonovic, D. Wielend, M. C. Scharber, *Mater. Adv.* **2021**, *2*, 4291.
- [50] Z. Hu, J. Wang, X. Ma, J. Gao, C. Xu, X. Wang, X. Zhang, Z. Wang, F. Zhang, *J. Mater. Chem. A Mater.* **2021**, *9*, 6797.
- [51] X. Ma, A. Zeng, J. Gao, Z. Hu, C. Xu, J. H. Son, S. Y. Jeong, C. Zhang, M. Li, K. Wang, H. Yan, Z. Ma, Y. Wang, H. Y. Woo, F. Zhang, *Natl. Sci. Rev.* **2021**, *8*, nwa305.
- [52] Y. Cai, Y. Li, R. Wang, H. Wu, Z. Chen, J. Zhang, Z. Ma, X. Hao, Y. Zhao, C. Zhang, F. Huang, Y. Sun, *Adv. Mater.* **2021**, *33*, 2101733.
- [53] H. C. Liao, C. C. Ho, C. Y. Chang, M. H. Jao, S. B. Darling, W. F. Su, *Mater. Today* **2013**, *16*, 326.
- [54] A. Zeng, X. Ma, M. Pan, Y. Chen, R. Ma, H. Zhao, J. Zhang, H. K. Kim, A. Shang, S. Luo, I. C. Angunawela, Y. Chang, Z. Qi, H. Sun, J. Y. L. Lai, H. Ade, W. Ma, F. Zhang, H. Yan, *Adv. Funct. Mater.* **2021**, *31*, 2102413.
- [55] P. Müller-Buschbaum, *Adv. Mater.* **2014**, *26*, 7692.
- [56] A. Mahmood, J. L. Wang, *Sol. RRL* **2020**, *4*, 2000337.
- [57] D. T. Nguyen, S. Sharma, S. A. Chen, P. V. Komarov, V. A. Ivanov, A. R. Khokhlov, *Mater. Adv.* **2021**, *2*, 1016.
- [58] S. V. Sujith, H. Kim, J. Lee, *Metals* **2022**, *12*, 165.
- [59] I. Caballero-Quintana, O. Amargós-Reyes, J. L. Maldonado, J. Nicasio-Collazo, D. Romero-Borja, D. Barreiro-Argüelles, G. Molnár, A. Bousseksou, *ACS Appl. Mater. Interfaces* **2020**, *12*, 29520.
- [60] F. Zhao, C. Wang, X. Zhan, *Adv. Energy Mater.* **2018**, *8*, 1703147.
- [61] Y. C. Liang, C. C. Wang, *RSC Adv.* **2018**, *8*, 5063.
- [62] D. Barreca, A. Gasparotto, C. Maragno, E. Tondello, T. R. Spalding, *Surf. Sci. Spectra* **2002**, *9*, 54.
- [63] S. Ren, L. Y. Chang, S. K. Lim, J. Zhao, M. Smith, N. Zhao, V. Bulović, M. Bawendi, S. Gradečak, *Nano Lett.* **2011**, *11*, 3998.
- [64] H. S. Lee, Y. W. Han, Y. C. Kim, J. Y. Kim, J. H. Kim, D. K. Moon, *ACS Appl. Energy Mater.* **2022**, *5*, 8400.
- [65] C. M. Proctor, T. Q. Nguyen, *Appl. Phys. Lett.* **2015**, *106*, 083301.
- [66] S. Li, L. Zhan, C. Sun, H. Zhu, G. Zhou, W. Yang, M. Shi, C. Z. Li, J. Hou, Y. Li, H. Chen, *J. Am. Chem. Soc.* **2019**, *141*, 3073.
- [67] Y. Wang, Z. Liang, J. Qin, J. Tong, P. Guo, X. Cao, J. Li, Y. Xia, *IEEE J. Photovolt.* **2019**, *9*, 1678.
- [68] W. E. I. Sha, X. Li, W. C. H. Choy, *Sci. Rep.* **2014**, *4*, 6236.
- [69] F. Liu, L. Zhou, W. Liu, Z. Zhou, Q. Yue, W. Zheng, R. Sun, W. Liu, S. Xu, H. Fan, L. Feng, Y. Yi, W. Zhang, X. Zhu, *Adv. Mater.* **2021**, *33*, 2100830.